10-1-2016

High-Temperature Corrosion Testing of Uranium Silicide Surrogates

B. J. Jaques
Boise State University

G. Alanko
Boise State University

D. P. Butt
Boise State University

ANS

NUCLEAR TECHNOLOGY · VOLUME 196 · 100–110 · OCTOBER 2016

High-Temperature Corrosion Testing of Uranium Silicide Surrogates

K. Urso,[a] K. Sridharan,[a] B. J. Jaques,[b,c] G. Alanko,[b,c] D. P. Butt,[b,c] M. Meyer,[d] P. Xu,[e] and B. Tyburska-Püschel[a]*

[a]*University of Wisconsin–Madison, Department of Engineering Physics, 1500 Engineering Drive, Madison, Wisconsin*
[b]*Boise State University, Department of Materials Science and Engineering, Boise, Idaho*
[c]*Center for Advanced Energy Studies, Idaho Falls, Idaho*
[d]*Idaho National Laboratory, Idaho Falls, Idaho*
[e]*Westinghouse Electric Company LLC, Pittsburgh, Pennsylvania*

Received December 7, 2015
Accepted for Publication May 9, 2016
http://dx.doi.org/10.13182/NT15-155

Abstract — *The corrosion resistance of cerium silicide, a surrogate of uranium silicide, is investigated to gain insight into the reaction of uranium silicide with water. As-received and proton-irradiated Ce_3Si_2, $CeSi_2$, and $CeSi_{1.x}$ monolithic pellets are subjected to corrosion tests in water at 300°C and 9 MPa for up to 48 h. Results show that an oxide layer composed of $Ce_{4.67}(SiO_4)_3O$ forms on the surface of all samples, and it grows thicker with extended exposure times. Irradiated samples corrode to a greater extent than their unirradiated counterparts, which is mainly a result of the existing post-irradiation cerium oxide and the presence of ion-induced defects. Most of the Ce_3Si_2 samples crack (as-received) or fracture (ion-irradiated) during testing, which is due to the brittleness of the samples and oxide erosion/spallation that occur during testing.*

Keywords — *Cerium silicide, water corrosion, surrogate.*

Note — *Some figures may be in color only in the electronic version.*

I. INTRODUCTION

The nuclear power industry has benefited from incremental system, equipment, and fuel design improvements that have increased efficiency and reliability of reactors. While these improvements have supplied small uprates and have kept nuclear power competitive, they seem to approach the maximum achievable impact within current material and regulatory constraints. To obtain higher uprates and increased efficiency, a fundamental change in the fuel needs to be made. Transitioning to a high-uranium-density fuel will allow for extended cycle lengths, large power uprates, and potential high burnups helping to meet growing electricity demands and contributing to the future sustainability of nuclear power.

Uranium silicide is one of the most promising high-uranium-density intermetallic fuels because of its advantageous thermal properties, irradiation performance, and accident tolerance.[1–3] U_3Si_2 boasts a uranium density of 11.31 g U/cm^3, which is nearly 20% U more than in UO_2, and it has a thermal conductivity that trends up with temperature opposed to down as seen with UO_2 (Ref. 4). Calculations have shown that at temperatures capable of melting UO_2 (T_m = 2850°C), the centerline temperature of U_3Si_2 (T_m = 1665°C) is 775°C lower than its melting point despite having a melting temperature almost 1200°C lower than UO_2 (Ref. 2). While the properties of these silicides show promise for use as advanced nuclear fuels, their reactivity in light water reactor (LWR) conditions needs to be better understood.

One such environment is when the coolant comes into contact with the fuel due to a cladding breach. Cladding

*E-mail: tyburska@engr.wisc.edu

breaches can occur during normal reactor operation due to fretting or pellet-cladding interactions or from embrittlement and cracking stemming from hydrogen production. Regardless of the cause, when a cladding breach occurs, the corrosion resistance of the fuel becomes important. If the fuel degrades rapidly, it can lose its structural integrity and be washed away by the circulating cooling water contaminating the primary loop. Such an accident would result in expensive cleanup costs and additional downtime for utilities. To avoid these problems, fuel must be stable in water, and its corrosion resistance should not be worse than that of UO_2 when exposed to the high pressures and temperatures associated with LWRs.

Many corrosion studies investigating uranium silicide primarily use dispersion fuels in research reactor conditions. These studies are performed by drilling a hole through the fuel plate and placing it in boiling water. Results from these tests showed that the solubility of several uranium silicides in water up to 100°C is negligible as no uranium is detected on the fuel plate surface after 150 h of testing.[5–7] Experiments that did use monolithic fuel at elevated temperatures are primarily focused on U_3Si because of its higher uranium density and its reported superior corrosion resistance in water. These studies found that a decrease in corrosion performance occurred due to the presence of free U (Refs. 8 and 9), U_3Si_2 (Ref. 10), or silicon content outside the range of 3.8 to 4.0 wt% (Refs. 8 and 10). With proper heat treatment of U_3Si, corrosion rates are found to be 0.07 to 0.14 mg/(cm^2 · h) at 260°C and 0.06 to 0.09 mg/(cm^2 · h) at 343°C and 15.2 MPa, which is substantially less than the 171 mg/(cm^2 · h) in 100°C water that is found for unalloyed uranium.[8,11] Further examination of U_3Si by Bourns[7,12] in water at 300°C and 12 MPa found that there is no trend in corrosion rate with silicon values between 3.6 and 4.0 wt%, which is in agreement with Howe and Bell.[13]

These corrosion studies only referenced the U_3Si_2 as fractional additions to U_3Si due to an excess amount of silicon added during the fabrication processes. While having excess silicon to convert free uranium to U_3Si_2 is beneficial, too much U_3Si_2 has been shown to be detrimental to the fuel's corrosion resistance.[9,14] Corrosion seems to be accelerated in areas surrounding U_3Si_2 particles. It is not fully understood why U_3Si preferentially hydrides to UH_3 (Ref. 15) around U_3Si_2, but it may be related to surface energies associated with the interphase or with differing diffusion rates. Reaction rates are derived from data from several experiments, and it is found that as-cast U_3Si_2 has a corrosion rate that is an intermediate between as-cast U_3Si and heat-treated U_3Si (Ref. 16). It is known that microstructure affects corrosion resistance and heat-treated U_3Si_2 may provide even greater corrosion resistance.

While previous studies have mentioned U_3Si_2 only as trace additions to U_3Si, few studies have focused solely on U_3Si_2. Two studies that did investigate pure U_3Si_2 found that it performs no worse than UO_2 pellets at 300°C and 9 MPa in water.[17,18] After 29 h of exposure, U_3Si_2 powder does not react to any more extent than UO_2 sintered pellets during the same exposure time despite the orders-of-magnitude difference in surface-to-volume ratio.[17] Additionally, U_3Si_2 sintered pellets between 85% and 87% theoretical density (TD) are tested, and after 29 h of exposure, the pellets did not hydrolyze to any more extent than UO_2 sintered pellets did after 1 h of exposure despite having lower TDs than the UO_2 pellets.[18] Further studies that are more representative of the water used in reactors need to be conducted to better understand the properties of these uranium silicides in water. However, investigation into surrogate materials can give additional insight with reduced cost and risk.

The use of surrogates in place of radioactive elements has several advantages including reduced risk and cost and the number of safety protocols that need to be in place. Cerium is chosen as a surrogate for uranium with these silicides because Ce_3Si_2 is isostructural with U_3Si_2 (Refs. 19, 20, and 21). Investigation into the thermodynamics of oxide formation using HSC Chemistry[22] shows that many $CeSi_2$ and USi_2 reactions in water are comparable. No comparison between Ce_3Si_2 and U_3Si_2 is made in this fashion as HSC Chemistry does not include many of the cerium silicide compounds. Table I shows the Gibbs free energies, enthalpies, and entropies for several similar reactions. These values show that these similar reactions are favored to occur for cerium and uranium silicides, further validating cerium silicide as a suitable surrogate for corrosion testing of uranium silicide fuels.

II. EXPERIMENTAL APPROACH

Three different compositions of cerium silicide are examined to determine their corrosion resistances. Both proton-irradiated and unirradiated Ce_3Si_2, $CeSi_2$, and $CeSi_{1.x}$ (x = 7 or 9) are tested at 300°C and 9 MPa (LWR's condition) in an Autoclave Engineers Inc. self-sealing flow-through autoclave (see Fig. 1) located at the Center for Advanced Energy Studies, Advanced Materials Laboratory, Idaho Falls. Tests are performed with a 3°C/min ramp-up rate and are allowed to air cool to room temperature. For each test 100 ml of deionized water is used. The autoclave is a 35-kg custom unit. The benchtop system consists of a Type 316 stainless steel pressure vessel enclosed in a ceramic band heater. The heater is

TABLE I

A Comparison of Gibbs Free Energies, Enthalpies, and Entropies for Several Reactions of USi_2 and $CeSi_2$*

Equation	ΔH (kJ)	ΔS (J/K)	ΔG (kJ)
$CeSi_2 + O_2(a) = CeO_2 + 2Si$	−1019	−405	−786
$USi_2 + O_2(a) = UO_2 + 2Si$	−1071	−373	−858
$CeSi_2 + 2O_2(a) = Ce + 2SiO_2$	−1870	−764	−1432
$USi_2 + 2O_2(a) = U + 2SiO_2$	−1929	−771	−1488
$USi_2 + O_2(a) = U + Si_2O_2(g)$	−401	−175	−301
$CeSi_2 + O_2(a) = Ce + Si_2O_2(g)$	−342	−169	−245
$e^- + CeSi_2 + 3OH(-a) + 4H(+a) = Ce(OH)_3 + Si_2H_4(g)$	−251	678	−639
$USi_2 + 4OH(-a) + 4H(+a) = U(OH)_4 + Si_2H_4(g)$	−268	879	−772
$CeSi_2 + 1.5OH(-a) + 2.75O_2(a) + 1.5H(+a) = Ce(OH)_3 + 2SiO_2$	−2936	−835	−2458
$USi_2 + 2OH(-a) + 3O_2(a) + 2H(+a) = U(OH)_4 + 2SiO_2$	−3138	−893	−2626
$2e^- + USi_2 + 4OH(-a) + 6H(+a) = U(OH)_4 + Si_2H_6$	−270	741	−695
$3e^- + CeSi_2 + 3OH(-a) + 6H(+a) = Ce(OH)_3 + Si_2H_6$	−253	539	−562
$6e^- + 2CeSi_2 + 3OH(-a) + 9H(+a) = Ce_2O_3 + 2Si_2H_6(g)$	−358	621	−714
$USi_2 + 3OH(-a) + 3H(+a) = UO_3 + Si_2H_6(g)$	−91	821	−561
$CeSi_2 + 2O_2(a) + 2H(+a) + 2e^- = CeH_2 + 2SiO_2$	−2067	−921	−1540
$USi_2 + 2O_2(a) + 3H(+a) + 3e^- = UH_3 + 2SiO_2$	−2062	−967	−1508

*From Ref. 22. Similar reactions occur for cerium and uranium silicides, validating cerium silicide as a uranium silicide surrogate.

rated for 1200 W and 120 VAC and can reach a maximum temperature of 800°C. The system's temperature is controlled by a UHC series control unit equipped with two Automations Direct Solo 4828 programmable controllers that monitor process temperature and heater/vessel overtemperature. The maximum allowable pressure is 38 MPa as regulated by a rupture disk safety valve. Figure 1 shows the side view of the autoclave with the main key components labeled. A detailed description of this unit as well as the standard operating procedure is included in Ref. 23.

The total elemental concentrations of Si and Ce in the aqueous sample (reported in units of micrograms per liter) are determined by magnetic-sector inductively coupled plasma–mass spectrometry (ICP-MS) after digestion of the samples with a mixture of high-purity acids. This testing was performed at the Environmental Chemistry & Technology and Wisconsin State Laboratory of Hygiene, University of Wisconsin–Madison.

Pellet sintering took place at the Boise State University Advanced Materials Laboratory. Powders were prepared by high-energy ball milling in a Retch PM100 planetary ball mill with stainless steel media of 5- and 10-mm diameters. A stainless steel medium was used over yttrium stabilized zirconia in an attempt to minimize contamination from the milling vessel during the milling process. Powders were milled for various times at 500 rpm to mechanically alloy the powder into the desired composition.[24] After milling, powder adhered to the milling media and vessel walls. To aid in the removal of this powder, hexane was added to the milling vessel and then milled for additional time. Samples made in this fashion failed within the first hour of corrosion testing, and this behavior is believed to be due to the addition of carbon from the hexane milling step. All subsequent milling runs were done without the addition of hexane. This change in technique resulted in samples that possessed far superior corrosion resistance as detailed in this work.

Prepared powders were cold pressed at 5 kN in a 21-mm die and then consolidated to high densities by spark plasma sintering (SPS). Samples were sintered for 15 min at a temperature of 75% of the melting point for each compound in a Dr. Sinter SPS-550. Sintered pellets were sectioned with a low-speed saw into smaller pieces and lightly polished to remove cutting fluids and other surface debris from sintering prior to corrosion testing. The density of all pellets is >95% TD as determined by both the Archimedes method and porosity measurements by scanning electron microscopy (SEM) combined with ImageJ (Ref. 25).

Proton-irradiation and post-irradiation examination were done at the University of Wisconsin–Madison using the facilities in the Characterization Laboratory for Irradiated Materials. Irradiation of 3-mm disks polished down to a thickness of <500 μm was performed with 2-MeV

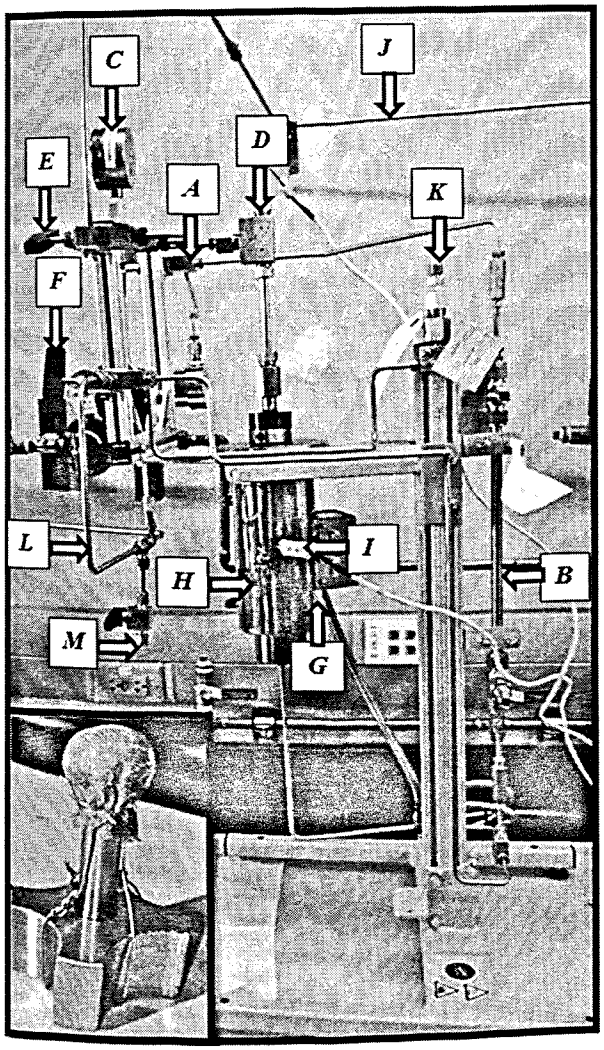

Fig. 1. Side view of the autoclave system with components labeled as follows: "*A*," gas outlet valve; "*B*," tube in tube heat exchanger; "*C*," pressure gauge; "*D*," fitting block; "*E*," gas inlet valve; "*F*," water outlet valve; "*G*," band heater; "*H*," pressure vessel; "*I*," heater/vessel thermocouple; "*J*," gas in line; "*K*," rupture disk valve; "*L*," water line to container; "*M*," water sampling valve. Left, bottom-corner inset: sample holder placed in the pressure vessel.

protons to a fluence of 3.9×10^{18} p/cm^2 at 400°C and 800°C with a damage rate of 3.9×10^{-6} displacements per atom (dpa)/s. The irradiation resulted in an implantation zone of 20 μm with a damage level of 0.5 dpa at 10 μm (see Fig. 2). SRIM 2013.00 (Ref. 26) is used along with the method proposed by Stoller et al.[27] to calculate the damage profile for Ce_3Si_2 using the Kinchin-Pease approach with displacement threshold energies of 25 and 15 eV from cerium and silicon,[26] respectively. SRIM reports an inaccurate TD for Ce_3Si_2, and a TD of 5.98 g/cm^3 is used in the calculations.[28] Usually, the extent of corrosion is

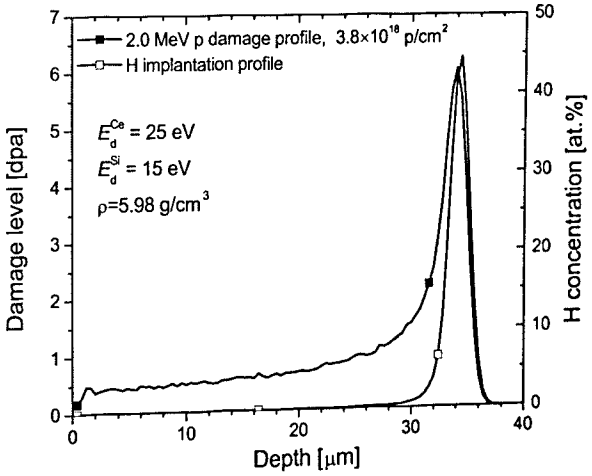

Fig. 2. Damage profile and H distributions in Ce_3Si_2 irradiated with 2.0-MeV protons to a damage level of 0.5 dpa at a depth of 10 μm. Calculations were performed using SRIM-2013.00 (Ref. 26), assuming the displacement threshold energies of 25 eV for Ce and 15 eV for Si.

estimated by measuring the sample mass change before and after the corrosion test with the existing (weight loss) or removed oxide layer (metal loss). However, because of sample fracturing and the subsequent loss of some material during testing, the determined corrosion rates (not shown) have limited values and do not reflect the true corrosion rates of the samples. Therefore, in this paper the extent of corrosion is judged by sample stability (fracturing and cracking) as well as the thickness of the oxide layer formed during the corrosion process.

Identification of the oxide layer formed on the surface was done by X-ray diffraction (XRD) on a Bruker D8 Discovery XRD with a Cu – K_α source (λ = 1.5418 Å). A 0.5-mm incident slit and collimator were used with a two-dimensional detector to collect $\theta - 2\theta$ scans at room temperature at the range between 20°C and 80°C with four steps (150 s/step) starting at 2θ = 20°C and increments of 20°C. Identical parameters were used for all investigated samples, and no background or K_{α_2} stripping was performed. The experimental XRD spectra were compared with the Inorganic Crystal Structure Database,[29] with the peak positions calculated for Cu – K_α, and for clarity, only peaks of intensity >10% I_{max} are shown. The half-value layers (penetration of X-rays) are 3.50 and 5.44 μm for Ce_3Si_2 and $CeSi_2$, respectively, which means that in the proton-irradiated samples, only the damaged layer is probed and not the substrate.

After corrosion testing, the samples were sectioned and mounted using a conductive mounting compound and a hot mounting press. The mounted samples were then polished with 1200 grit silicon carbide paper with further polishing being done with diamond paste. SEM and

energy dispersive spectroscopy (EDS) analysis along the sample's cross section was done on a JEOL JSM-6610 scanning electron microscope, and data were used to determine the maximum thickness of the oxide layer. Several low-count-rate (high-resolution) EDS line scans were completed on all four sides of each sample starting from the mount material, continuing through the oxide layer, and finishing in the bulk material. Elemental data were collected using an EDS detector and quantified using the ZAF method to show the cerium silicide composition as a function of cross-sectional distance. The oxide layer thickness is found by determining where the oxygen concentration surpassed the average oxygen level in the bulk material and in the mount material. Only the thickest oxide layers found are presented in this work because oxide growth, erosion, and cracking (see Fig. 3), which can possibly lead to oxide spallation, are competing phenomena, and thinner oxide layers do not represent the extent of corrosion. Erosion is expected as the oxide layer grows thicker and material on the surface can be removed by circulating water.

III. REACTION OF Ce_xSi_y WITH WATER: RESULTS AND DISCUSSION

III.A. Samples Prior to Corrosion Testing

Prior to testing, XRD analysis performed on all samples shows that samples from all three stoichiometries are nearly phase pure[24] (also see Figs. 4a and 5a, black lines with full squares). The 2-MeV proton irradiation leads to CeO_2 formation on the surface of the Ce_3Si_2 samples, while no oxidation of $CeSi_2$ and $CeSi_{1.x}$ (x = 7 or 9) is observed.[28]

III.B. Ce_3Si_2 Water Corrosion

Six unirradiated Ce_3Si_2 samples are corrosion tested: two each for 1, 12, and 24 h. Slight mass gains and positive corrosion rates are observed only in the shortest tests, while mass losses are observed in the longer tests. These losses occur because large pieces of the samples fracture off during testing (as-received samples) or the

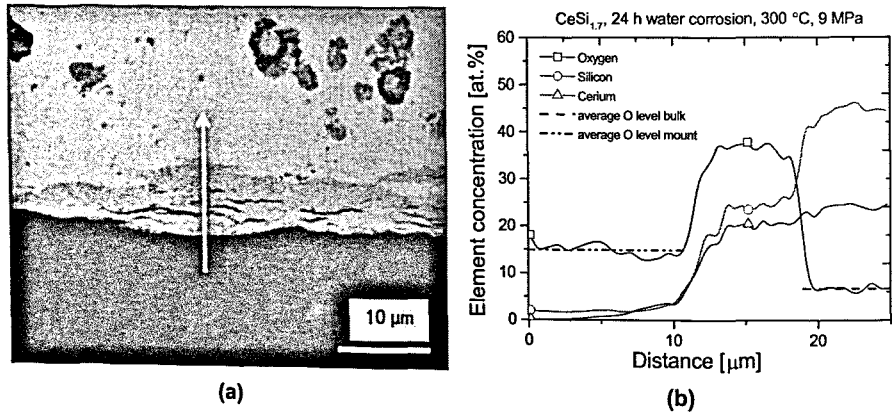

Fig. 3. (a) Backscattered electron detector–SEM image showing the oxide layer formed on the outer edge of the 24-h corrosion-tested $CeSi_{1.7}$ and (b) the corresponding EDS line scan showing the oxide layer thickness.

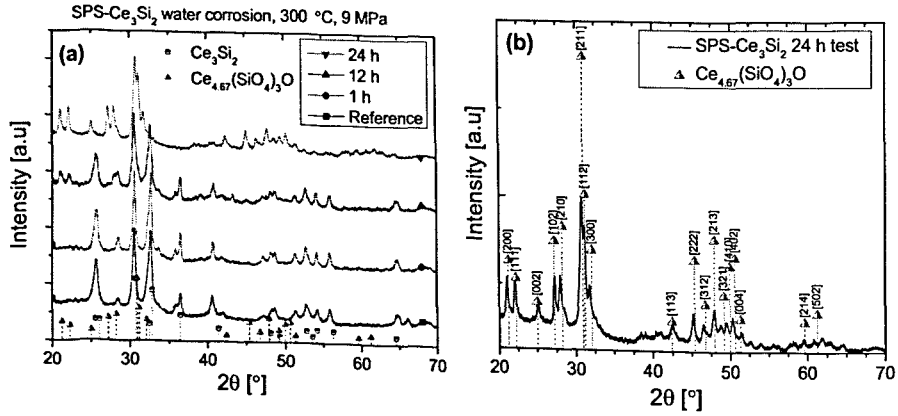

Fig. 4. XRD analysis of the SPS-Ce_3Si_2 samples after water corrosion test conducted at 300°C and 9 MPa for up to 24 h. The results show the formation of $Ce_{4.67}(SiO_4)_3O$ (pdf 00-043-0441) (Ref. 30). The lack of substrate signal indicates that the oxide thickness is greater than the X-ray penetration depth of ~3.5 µm.

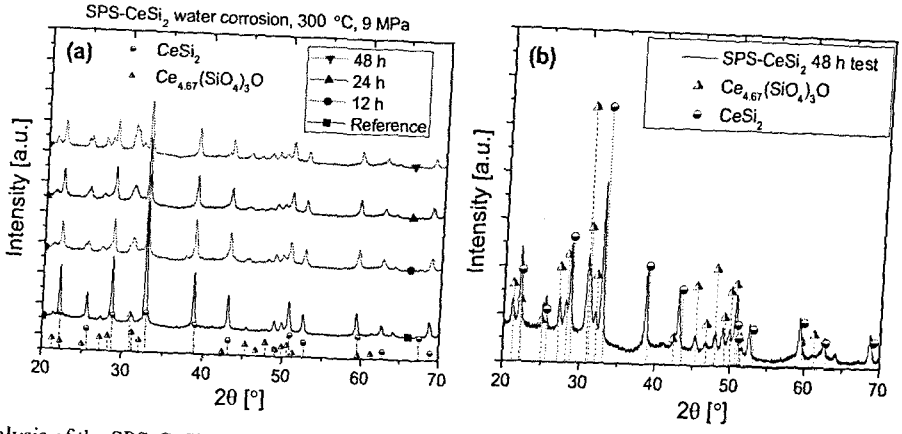

Fig. 5. XRD analysis of the SPS-$CeSi_2$ samples after water corrosion test conducted at 300°C and 9 MPa for up to 48 h. The results show the formation of $Ce_{4.67}(SiO_4)_3O$ (pdf 00-043-0441) (Ref. 30). The presence of substrate signal indicates that the oxide thickness is lower than the X-ray penetration depth of ~5.44 μm.

samples turn into dust (see Table II). This behavior is believed to be due to the brittleness of the as-received Ce_3Si_2 samples. Internal stresses coupled with the stress applied by the oxide layer may have been enough to cause the larger pieces to fracture off in a brittle fashion.

The maximum oxide layer thickness increases with extended exposure times and reaches a maximum of 4.9 μm after 24 h. XRD analysis (see Fig. 4a) shows the evolution of the oxide layer formation with corrosion time with the oxide being identified as hexagonal cerium oxide apatite $Ce_{4.67}(SiO_4)_3O$ (Ref. 30) (see Fig. 4b). This oxide forms through the reaction of two binary oxides CeO_2 and SiO_2.

Rewriting the oxide layer composition (divide by a factor 4.67/3 = 1.56) to more closely represent the Ce_3Si_2 composition, it turns into $Ce_3Si_{1.93}O_{8.35}$. From this, it can be seen that there is a slight loss of silicon content and a large gain in oxygen content. Substantial oxide formation starts after 12 h of water corrosion and continues such that after 24 h the oxide is thick enough that the substrate signal is no longer detected by XRD (see Fig. 4b). The X-ray penetration depth in $Ce_{4.67}(SiO_4)_3O$ (density ρ = 5.47 g/cm³) (Ref. 31) is 4.83 μm, and the oxide thicknesses measured by XRD and EDS are in good agreement, which means the oxide thickness is fairly uniform.

Two Ce_3Si_2 samples irradiated to 0.5 dpa at 800°C are corroded for 12 and 24 h. One Ce_3Si_2 sample, irradiated to 0.5 dpa at 400°C, is tested for 24 h. One edge of the sample irradiated to 0.5 dpa at 800°C for 12 h fractures off during testing, while the sample irradiated to 0.5 dpa at 800°C for 24 h fails completely, breaking up into fine dust with only small fragments remaining (see Table II). The sample irradiated to 0.5 dpa at 400°C tested for 24 h nearly breaks in half during testing, and multiple cracks are seen when investigating with an optical microscope. Higher-temperature irradiation accelerates the fracturing process, and the 400°C irradiated sample would possibly break apart in a similar fashion as the 800°C sample given additional exposure time.

The mobility of defects, especially vacancies, depends on the temperature, and it is expected that higher temperatures would lead to formation of more complex defects like vacancy clusters and voids. The melting temperature of Ce_3Si_2 is T_m = 1608 K and of $CeSi_2$ is T_m = 1893 K (Ref. 19), which means that all irradiations were performed at the homologous temperatures above $0.3T_m$, i.e., at temperatures that would lead to three-dimensional defect formation. We have no microstructure data from transmission electron microscopy to support this hypothesis, but it is expected that especially the 800°C irradiation leads to formation of a microstructure populated with voids and even nanopores, which causes a complete sample failure.

Maximum oxide layer thicknesses for irradiated samples are thicker than unirradiated counterparts and reach a maximum of 8.84 μm with the sample irradiated to 0.5 dpa at 400°C after 24 h of corrosion. The thickness of the oxide layer of the sample irradiated to 0.5 dpa at 800°C cannot be measured but is believed to have been thicker because of the manner in which the sample failed. No post-test XRD is performed on irradiated samples as the samples are consumed during the mounting process. Proton irradiation increases the brittleness of the samples as irradiated Ce_3Si_2 samples performed worse than unirradiated samples from a mechanical integrity standpoint. The increased brittleness may be due to the presence of post-irradiation CeO_2 (Ref. 28), which leads to faster formation of $Ce_{4.67}(SiO_4)_3O$.

III.C. $CeSi_2$ Water Corrosion

Three unirradiated $CeSi_2$ samples are exposed for 12, 24, and 48 h. All samples remain completely intact with

TABLE II

Optical Images of Unirradiated and Proton-Irradiated SPS-Ce_3Si_2, SPS-$CeSi_2$, and SPS-$CeSi_{1.x}$ Before (Left) and After (Right) the Water Corrosion Test Conducted at 300°C and 9 MPa at Various Times*

Corrosion Time	SPS-Ce_3Si_2	SPS-$CeSi_2$	SPS-$CeSi_{1.x}$
1 h	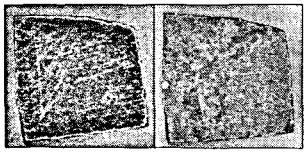	Not tested	Not tested
12 h	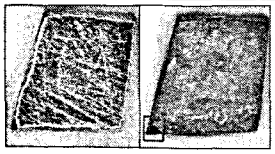	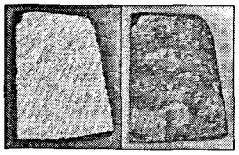	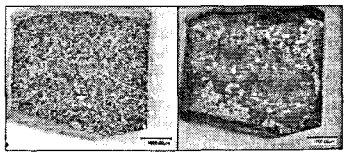
24 h	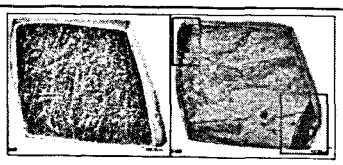	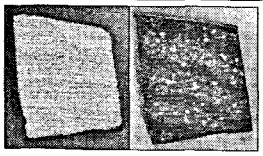	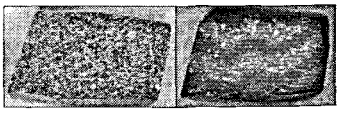
48 h	Not tested	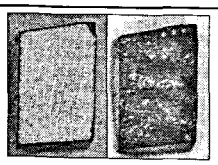	Not tested
Proton-Irradiated Samples			
12 h	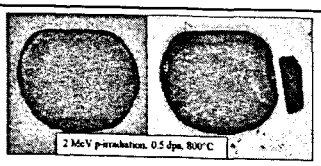	Not tested	Not tested
24 h	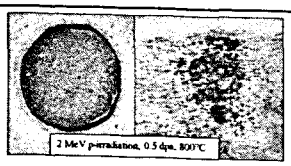	Not tested	Not tested
24 h	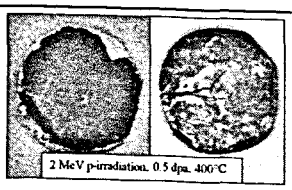	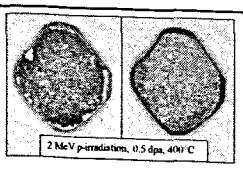	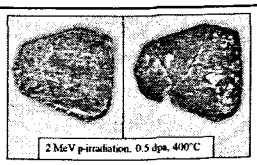

*Red frames (color online) mark locations were pieces of material fell off. The 1-mm scale bar shown for the SPS-$CeSi_{1.x}$ and 12-h sample applies to all images. $CeSi_2$ shows higher resistance to water corrosion than Ce_3Si_2 with prolonged exposure times.

only a darkening in color visible on the surface as seen in Table II. The maximum oxide layer thickness for each time interval is less than that for the corresponding Ce_3Si_2 tests, and it increases with the exposure time (see Fig. 6). XRD analysis shows that the oxide layer formed is the same $Ce_{4.67}(SiO_4)_3O$ (or rewritten as $CeSi_{0.64}O_{2.8}$) and,

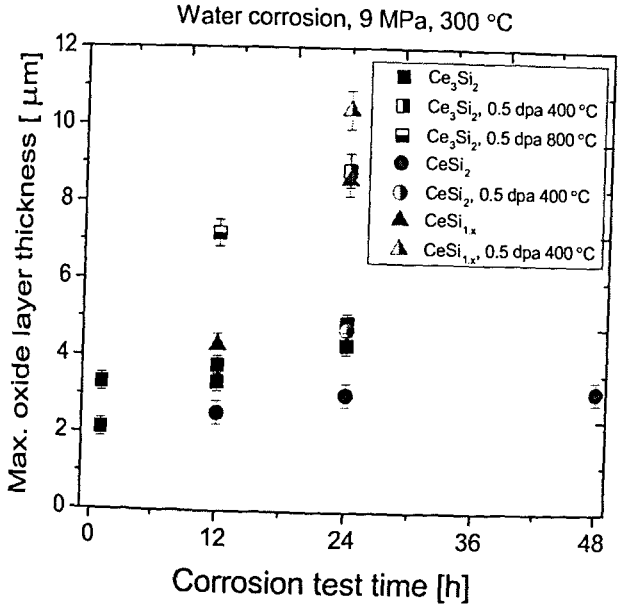

Fig. 6. Maximum oxide layer thickness for all Ce-Si samples exposed to water at 300°C and 9 MPa. $CeSi_2$ performs better than Ce_3Si_2, and proton irradiation has accelerated the corrosion process.

unlike Ce_3Si_2, the substrate signal is detected even after the 48-h test (see Fig. 5b). XRD pattern evolution with corrosion time shows almost no signs of surface oxidation after the 24-h tests and only slight oxidation after 48 h. This result is in contrast to the maximum oxide layer thickness measured by EDS (see Fig. 6), which indicates a nonuniform oxide distribution. XRD analysis can provide some insight as to the uniformity of the oxide as this technique is sensitive to an average oxide thickness.

At the same corrosion conditions, $CeSi_2$ samples perform better than Ce_3Si_2 samples with no fracturing or cracking and thinner maximum oxide layer formation. This shows a slower oxide layer growth or different corrosion mechanism in $CeSi_2$ than in Ce_3Si_2 samples, and it agrees with maximum oxide layer thickness measurements by EDS shown in Fig. 6. A maximum oxide layer thickness of 3.15 μm is found after 48 h of testing.

One $CeSi_2$ sample is irradiated to 0.5 dpa at 400°C and tested for 24 h. This sample shows only a slight darkening of the surface and has no fractures or deformations (see Table II). Surface features visible pretest are also seen post-test. The maximum oxide layer thickness is larger than the 24-h unirradiated sample with the thickest oxide layer ~4.71 μm (see Fig. 6).

The behavior of slower oxidation of $CeSi_2$ is expected since oxidation studies on Ce_3Si_2 have shown that secondary particles of $CeSi_2$ form and retard further oxidation. $CeSi_2$ samples are not as brittle as Ce_3Si_2 samples and maintain integrity throughout testing. While some cerium density is being forfeited in this compound, its corrosion resistance is superior and may still possess favorable properties justifying USi_2 as a replacement for UO_2. Proton-irradiated $CeSi_2$ performs better than Ce_3Si_2 possibly because $CeSi_2$ does not experience post-irradiation oxide formation as reported by Reinicke et al.[28] However, proton-irradiated $CeSi_2$ experiences greater surface oxidation than its unirradiated counterpart, which is probably caused by the presence of ion-induced defects.

III.D. $CeSi_{1.x}$ Water Corrosion

Two unirradiated $CeSi_{1.x}$ samples are tested for 12 and 24 h, and one $CeSi_{1.x}$ sample irradiated to 0.5 dpa at 400°C is tested for 24 h. All samples remain intact with no fractures, similar to $CeSi_2$ samples (see Table II). The fracture of the proton-irradiated sample occurs post-corrosion during sample removal from the pressure vessel.

Maximum oxide layer thickness measurement by EDS (see Figs. 3 and 6) shows the formation of a thicker oxide layer for longer exposure times and its rapid growth for irradiated samples (see Fig. 6). Cracks in oxide are observed (see Fig. 3), which could lead to oxide spallation. XRD analysis once again shows the formation of a $Ce_{4.67}(SiO_4)_3O$ oxide layer, but even after a 24-h test, the substrate signal is still detected, which indicates a non-uniform oxide thickness. The maximum oxide thickness observed by EDS is <5 μm, but the substrate signal is still detected by XRD, which confirms that the oxide thickness is not uniform. That is why the $CeSi_{1.x}$ samples did not fracture despite the fact that they have comparable or higher maximum oxide thicknesses compared to Ce_3Si_2 samples. $CeSi_{1.x}$ sample oxide layers are thicker than Ce_3Si_2 and $CeSi_2$ for both unirradiated and irradiated samples, but the integrity of the samples is comparable to that of $CeSi_2$ as no fracturing is observed.

Optical images reveal reflective flakes of what is hypothesized to be silicon dioxide that is not seen on other samples (see Fig. 7). These particles appear only on the $CeSi_{1.x}$ samples, and the number density of these particles increases with the corrosion time. Existence of this oxide is a prerequisite for the formation of $Ce_{4.67}(SiO_4)_3O$. Because silicon dioxide is amorphous, we are unable to confirm its presence using XRD. Also, we were not able to analyze those flakes using EDS as they are not reflective under SEM and therefore are very difficult to localize.

As seen in Table II, five out of six Ce_3Si_2 samples experienced various degrees of cracking, and no cracking was observed in the $CeSi_2$ or $CeSi_{1.x}$ samples. On the other hand, unlike Ce_3Si_2, the $CeSi_2$ and $CeSi_{1.x}$ samples display

uneven oxide distribution, which could mean that they experienced local oxide spallation. This could be either due to the brittleness of the bulk material further enhanced by proton irradiation (no literature data are available on the hardness of those compounds) or due to the stress applied by the oxide layer that could stem from the lattice mismatch of the bulk material and the oxide. As shown in Table III, the $Ce_{4.67}(SiO_4)_3O$ oxide has a different crystal system than the bulk materials, and there is a large mismatch between lattice parameters. Such lattice discrepancy could have an influence on the brittleness of the material.

Figure 6 shows measured maximum oxide layer thicknesses against time tested. A general trend of increasing oxide thickness with increased exposure time is seen for all three compounds. In all cases irradiated samples possess a thicker corrosion layer than their unirradiated counterparts. This is connected to the known phenomena of irradiation-assisted corrosion and irradiation-assisted stress corrosion cracking,[32] which enhance the material susceptibility to both corrosion and cracking. However, both mechanisms, especially stress corrosion cracking, are not yet fully understood, and the final corrosion/cracking results might differ between irradiation-corrosion experiments performed subsequently or simultaneously.[33] The extent of this difference is unknown at this moment as there are only a few facilities that are able to perform simultaneous ion-irradiation and water corrosion.

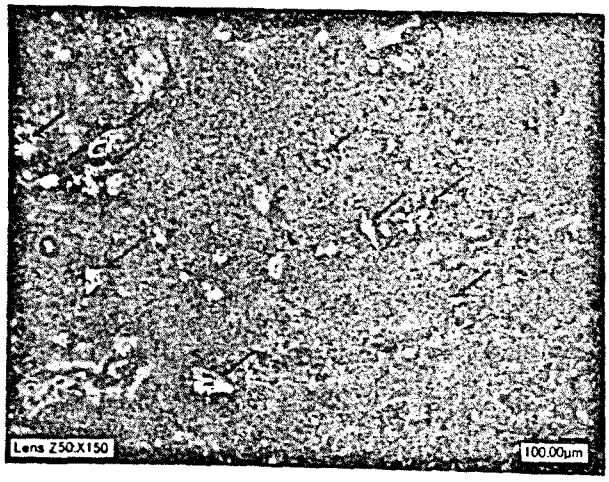

Fig. 7. Optical image of unirradiated SPS-$CeSi_2$ sample (24-h test, 300°C, and 9 MPa) showing reflective flakes (marked with arrows), which are believed to be SiO_2.

III.E. ICP-MS Test Results

An oxide layer of $Ce_{4.67}(SiO_4)_3O$ was formed on the surface of all tested samples. In the case of Ce_3Si_2, this means that there is a small loss of silicon and a large gain in oxygen content. For $CeSi_2$ and $CeSi_{1.x}$, there is a large loss in silicon content and a small gain in oxygen. As was confirmed by the ICP-MS test for Ce_3Si_2 and $CeSi_2$, the excess silicon leached into water.

Figure 8 shows the ratio of cerium to silicon in the post-corrosion water. If both cerium and silicon would erode evenly, then the ratio of cerium to silicon would be 1.5,

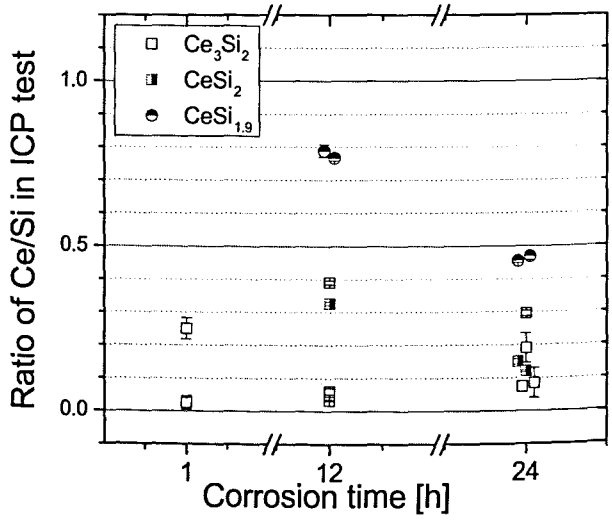

Fig. 8. Ratio of cerium to silicon measured by ICP test in the post-corrosion water for Ce_3Si_2, $CeSi_2$, and $CeSi_{1.9}$ samples. No distinction is made between as-received and irradiated samples. For even erosion the ratio of Ce/Si would be 1.5, 0.5, and 0.53 for Ce_3Si_2, $CeSi_2$, and $CeSi_{1.9}$, respectively.

TABLE III

Crystal Systems and Lattice Constants of All Studied Compounds

Compound	Crystal System	*a* (Å)	*c* (Å)	Reference
Ce_3Si_2	Tetragonal	7.79	4.36	19
$CeSi_2$	Tetragonal	4.19	13.90	29
$CeSi_{1.9}$	Tetragonal	4.19	13.89	29
$CeSi_{1.7}$	Orthorombic	4.10	13.82	29
$Ce_{4.67}(SiO_4)_3O$	Hexagonal	9.66	7.12	30

0.5, and 0.53 for Ce_3Si_2, $CeSi_2$, and $CeSi_{1.9}$, respectively. Especially for Ce_3Si_2, it can be seen that more Si leached into water (~80% to 95%) than one would expect from its stoichiometry (40 at. %) if Si and Ce would erode evenly. The ratio of cerium to silicon for $CeSi_2$ is only slightly below 0.5, which means that like for Ce_3Si_2, more Si leached into water, but the difference between the erosion strength of Ce and Si is not as pronounced as for Ce_3Si_2. For $CeSi_{1.9}$, the silicon concentration in the water is comparable to its content in this compound because the excess Si did not leach into water but precipitated on the sample surface in the form of the silicon dioxide flakes. The detected cerium-to-silicon ratio is independent of the pre-irradiation history of the tested samples.

IV. SUMMARY

Unirradiated and irradiated Ce_3Si_2, $CeSi_2$, and $CeSi_{1.x}$ pellets are water corrosion tested at 300°C and 9 MPa for up to 48 h. Performance of these compounds is evaluated by the integrity of the samples post-test and the observed maximum oxide layer thickness. Conclusions drawn from this work are the following:

1. As-fabricated Ce_3Si_2 fractures during testing.

2. $CeSi_2$ performs better than Ce_3Si_2 from the standpoints of integrity and maximum oxide thickness.

3. $CeSi_{1.x}$ shows the thickest maximum oxide layer and formation of silicon dioxide on the surface, but the XRD results indicate that the oxide thickness is not uniform (average oxide thickness is lower), which prevents the samples from cracking.

4. Irradiation promotes accelerated oxide layer growth.

5. The oxide layer formed on all compounds is that of $Ce_{4.67}(SiO_4)_3O$.

From the obtained data it is concluded that $CeSi_2$ is the most corrosion resistant of the tested compounds. It possessed the thinnest oxide layer and maintained its integrity throughout testing. Ce_3Si_2 did not perform to any appreciable extent worse than $CeSi_2$ for the thickness of the oxide layer; however, it did suffer from fracturing during testing and needs to be mechanically strengthened for future research. While Ce_xSi_y testing may provide insights into how U_xSi_y will react, further studies using uranium compounds are required to validate its potential use in commercial reactors. If Ce_xSi_y is found to be a suitable surrogate for U_xSi_y, then USi_2 may be the preferred candidate for further studies due to its enhanced corrosion resistance.

Acknowledgments

This project is supported by the U.S. Department of Energy under Nuclear Energy University Program award 11-3041. The instrumentation support is provided by National Science Foundation grant DMR-1121288.

References

1. M. FINLAY, G. HOFMAN, and J. SNELGROVE, "Irradiation Behaviour of Uranium Silicide Compounds," *J. Nucl. Mater.*, **325**, 118 (2004); http://dx.doi.org/10.1016/j.jnucmat.2003.11.009.
2. E. LAHODA, "U_3Si_2 Evaluation," Westinghouse Electric Company (2012).
3. J. SNELGROVE et al., "Development of Very-High-Density Low-Enriched-Uranium Fuels," *Nucl. Eng. Des.*, **178**, 119 (1997); http://dx.doi.org/10.1016/S0029-5493(97)00217-3.
4. J. WHITE et al., "Thermophysical Properties of U_3Si_2 to 1773 K," *J. Nucl. Mater.*, **464**, 275 (2015); http://dx.doi.org/10.1016/j.jnucmat.2015.04.031.
5. T. WIENCEK, "Summary Report on Fuel Development and Miniplate Fabrication for the RERTR Program," ANL/RERTR/TM-15, Argonne National Laboratory (1995).
6. J. SNELGROVE et al., "The Use of U_3Si_2 Dispersed in Aluminum in Plate-Type Fuel Elements for Research and Test Reactors," ANL/RERTR/TM-11, Argonne National Laboratory (1987).
7. W. BOURNS, "Corrosion Testing of Uranium Silicide Fuel Specimens," AECL-2718, Atomic Energy of Canada Limited (Sep. 1968).
8. S. ISSEROW, "The Uranium-Silicon Epsilon Phase," *J. Met.*, **9**, 1236 (1957).
9. J. McWHIRTER, "Aqueous Corrosion of Uranium and Alloys: Survey of Project Literature," ANL-4862, Argonne National Laboratory (1952).
10. R. WOLFE, "Development of U_3Si Epsilon Phase Alloys for Use in Pressurized Water Reactors," Westinghouse Atomic Power Division (1956).
11. A. RITCHIE, "A Review of the Rates of Reaction of Uranium with Oxygen and Water Vapour at Temperatures up to 300°C," *J. Nucl. Mater.*, **102**, 170 (1981); http://dx.doi.org/10.1016/0022-3115(81)90557-2.
12. W. BOURNS, "A Literature Survey of U_3Si Corrosion," AECL-2609, Atomic Energy of Canada Limited (July 1965).
13. L. HOWE and L. BELL, "Pre-Irradiation Tests on U-Si Alloys," CR-Met-763, Atomic Energy of Canada Limited (May 1958).
14. W. WILKINSON, *Uranium Metallurgy*, Interscience Publishers, New York (1962).

15. M. FERADAY, "The Oxidation, Hydriding and Aqueous Corrosion of U_3Si Alloys," AECL-3862, Atomic Energy of Canada Limited (Nov. 1971).

16. B. HILTON, "Review of Oxidation Rates of DOE Spent Nuclear Fuel," ANL-00/24, Argonne National Laboratory (2000).

17. "Final Report on the Interaction Between Triuranium Disilicide Powder and Water," INVAP, 0909-WHUN-3BEIN-035-A, Westinghouse Electric Company (2009).

18. "Final Report on the Interaction Between Triuranium Disilicide Pellets and Water," INVAP, 0909-WHUN-3BEIN-038, Westinghouse Electric Company (2011).

19. M. BULANOVA et al., "Cerium-Silicon System," *J. Alloys Compd.*, **345**, 110 (2002); http://dx.doi.org/10.1016/S0925-8388(02)00409-7.

20. B. PREDEL, *Ce-Si: Phase Equilibira Crystallographic and Thermodynamic Data of Binary Alloys*, Springer, Berlin (2000).

21. A. SHUKLA, Y.-B. KANG, and A. PELTON, "Thermodynamic Assessment of the Ce-Si, Y-Si, Mg-Ce-Si and Mg-Y-Si Systems," *Int. J. Mater. Res.*, **100**, 2 (2009); http://dx.doi.org/10.3139/146.110003.

22. HSC Chemistry Web Site (2015): http://www.hsc-chemistry.net (current as of Dec. 7, 2015).

23. K. URSO, "Corrosion Studies of Cerium Silicides as Surrogates for Uranium Silicides," Master Thesis, University of Wisconsin–Madison (2014).

24. G. ALANKO et al., "Mechanochemical Synthesis and Spark Plasma Sintering of the Cerium Silicides," *J. Alloys Compd.*, **616**, 306 (2014); http://dx.doi.org/10.1016/j.jallcom.2014.07.129.

25. ImageJ Web Site (2015): http://www.imagej.net (current as of Dec. 7, 2015).

26. SRIM Web Site (2015): http://www.srim.org/ (current as of Dec. 7, 2015).

27. R. STOLLER et al., "On the Use of SRIM for Computing Radiation Damage Exposure," *Nucl. Instrum. Methods Phys. Res. B*, **310**, 75 (2013); http://dx.doi.org/10.1016/j.nimb.2013.05.008.

28. A. REINICKE et al., "Densification and Thermal Conductivity of Proton Irradiated Cerium Silicide," *J. Nucl. Mater.* (submitted for publication).

29. Inorganic Crystal Structure Database Web Site, FIZ Karlsruhe (2015): https://icsd.fiz-karlsruhe.de (current as of Dec. 7, 2015).

30. A. TAS and M. AKINC, "Cerium Oxide Apatite ($Ce_{4.67}(SiO_4)_3O$) X-Ray Diffraction Pattern Revisited," *Powder Diffr.*, **7**, 219 (1992); http://dx.doi.org/10.1017/S0885715600018753.

31. A. TAS and M. AKINC, "Phase Relations in the System Ce_2O_3-$Ce_2Si_2O_7$ in the Temperature Range 1150° to 1970°C in Reducing and Inert Atmospheres," *J. Am. Ceram. Soc.*, **77**, 2953 (1994); http://dx.doi.org/10.1111/j.1151-2916.1994.tb04530.x.

32. G. WAS and P. ANDRESEN, "Irradiation Assisted Corrosion and Stress Corrosion Cracking (IAC/IASCC) in Nuclear Reactor Systems and Components," *Nucl. Corros. Sci. Eng.*, **6**, 131 (2012); http://dx.doi.org/10.1533/9780857095343.2.131.

33. S. RAIMAN et al., "A Facility for Studying Irradiation Accelerated Corrosion in High Temperature Water," *J. Nucl. Mater.*, **451**, 40 (2014); http://dx.doi.org/10.1016/j.jnucmat.2014.03.022.